ACSNANO

www.acsnano.org

Three-Dimensional Printing Ultrastrong, Ultraductile Micro/nano Silicon Oxycarbide Ceramics Derived from a Monolithic Preceramic Resin

Gan Luo,[§] Yuan Tao,[§] Jincheng Ni, Modong Jiang, Feng Tang, Yanlei Hu, Dong Wu, Jiaru Chu, and Jiawen Li*

Cite This: https://doi.org/10.1021/acsnano.6c02930

Read Online

ACCESS | Metrics & More | Article Recommendations | Supporting Information

ABSTRACT: **Polymer-derived ceramics (PDCs) are promising candidates for fabricating three-dimensional (3D) micro/nanodevices. However, their advancement has been constrained by a persistent challenge in that precursor simplicity, high-fidelity shaping of complex 3D architectures, and superior mechanical properties in the final ceramic are incompatible. To overcome this, an extremely simple photosensitive preceramic resin comprising only polycarbosilane and a photoinitiator is proposed to fabricate high-precision 3D PDC microstructures with intricate geometries and exceptional mechanical performance. A process involving prebaking and two-photon polymerization forms stable 3D preceramic polymer networks, which after pyrolysis yield defect-free amorphous SiOC ceramics exhibiting high shape fidelity and low linear shrinkage (28% at 1000 °C). The ceramics show temperature-dependent mechanical properties, with micropillar compressive strength reaching 6.41 GPa (1000 °C) and 7.55 GPa (1200 °C). Leveraging these properties, lightweight high-strength mechanical metamaterials with 20% relative density are fabricated, achieving a compressive strength of 0.54 GPa and a failure strain exceeding 10%. Functional microneedle arrays are also produced, highlighting their potential for biomedical applications. This work establishes a reliable and straightforward route from an extremely simple precursor to high-performance PDC micro/nano devices, showcasing promising prospects for applications in advanced microsystems and lightweight metamaterials.**

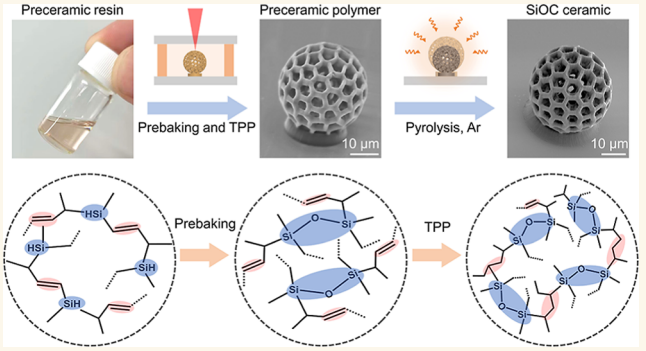

KEYWORDS: *polymer-derived ceramics, two-photon polymerization, SiOC, nanolattice, 3D printing, mechanical metamaterials*

Three-dimensional (3D) micro/nano devices are evolving toward functional integration and structural complexity.[1−4] Ceramic materials, owing to their excellent mechanical strength and chemical stability, are ideal candidates for constructing high-performance 3D micro/nanodevices, the realization of which relies on advanced manufacturing technologies.[5−9] Concurrently, polymer-derived ceramics (PDCs) technology has emerged as a powerful approach for synthesizing and shaping ceramics.[10−12] Ceramic precursors possess a unique molecular designability. Through chemical modification with photocurable groups such as acrylates or vinyl groups, they enable the precise shaping of complex 3D architectures at the polymer stage, which are subsequently converted into final ceramic components via heat treatment. This characteristic makes them especially suitable for photopolymerization-based manufacturing processes.[13−16] Among available techniques, two-photon polymerization (TPP) stands out for its exceptional resolution and free-form 3D shaping capability, making it an ideal tool for fabricating high-precision ceramic micro/nanostructures, with successful applications already demonstrated in mechanical metamaterials, photonic crystals, and related fields.[1,17−22] Therefore, the combination

Received: February 13, 2026
Revised: June 19, 2026
Accepted: June 22, 2026

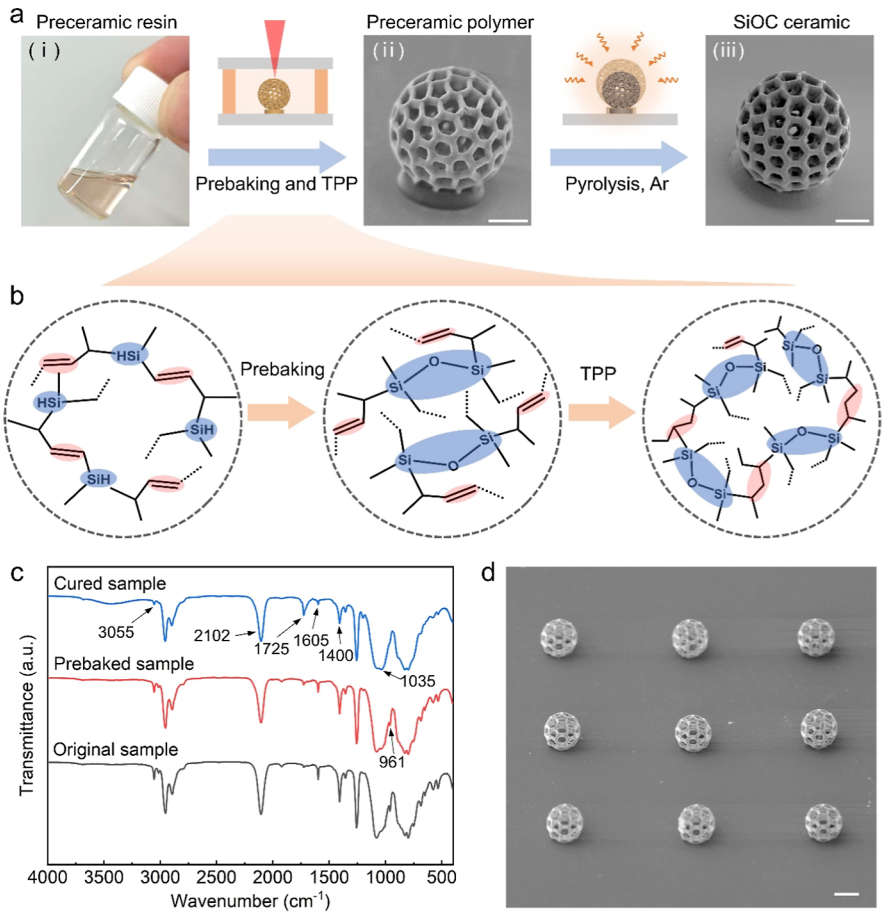

Figure 1. General process for fabricating PDC microstructures and TPP mechanism of photosensitive preceramic resin. (a) The process of fabricating PDC microstructures through prebaking, TPP, and pyrolysis. Scale bars, 10 μm. (b) Molecular structural changes during prebaking and TPP. (c) FTIR spectra of the original, prebaked, and cured samples. (d) SEM images of the printed 3D preceramic polymer array. Scale bar, 20 μm.

of TPP and PDC technology provides a new and powerful pathway for producing 3D micro/nano ceramic devices.

Although significant advances have been made in fabricating 3D micro/nano devices via TPP-PDC technology, its development continues to face a persistent challenge, namely, achieving synergy among precursor simplicity, high shape fidelity during pyrolysis, and exceptional mechanical properties in the final ceramic within a single material system.[23−25] Existing studies have typically managed to balance only one or two aspects. Earlier work focuses primarily on demonstrating the feasibility of PDCs for micro/nano 3D fabrication and exploring suitable fundamental material systems. For example, Pham et al. and Park et al. introduce external phases such as SiO_2 particles or organometallic additives to mitigate deformation and preserve morphology, yet overall printing accuracy and 3D fidelity remain limited.[23,24] More recent research has shifted toward performance enhancement, yielding several breakthroughs, including the realization of ultrahigh plasticity or strength at micro/nano scales, reduction of linear shrinkage to around 30%, and preparation of ceramics suitable for high-temperature applications.[26−28] While these contributions have pushed PDC technology forward in 3D micro/nano fabrication, the triple goals of simple precursors, high 3D shape fidelity, and ultrahigh mechanical performance have not been simultaneously attained. In particular, a minimal material system is desirable to reduce production costs, maximize ceramic yield, minimize material loss, and control shrinkage. Therefore, developing a novel precursor system that combines a single-component formulation, high 3D shape fidelity, and extraordinary mechanical properties has become the key to breaking the current bottleneck of TPP-PDC technology and unlocking its broad application potential.

Here, we propose a fabrication method for PDC microstructures based on an extremely simple photosensitive preceramic resin. This resin consists solely of polycarbosilane and a photoinitiator, offering excellent stability while significantly reducing preparation complexity and cost. Through a two-step cross-linking process involving prebaking followed by two-photon polymerization, the network density within the preceramic polymer is enhanced, enabling the successful construction of stable 3D microstructures. Subsequent pyrolysis converts these structures into homogeneous amorphous SiOC ceramics that are free of defects and exhibit high shape fidelity and low linear shrinkage of only 28% after pyrolysis at 1000 °C. The minimum feature size of the ceramic microstructure can reach 200 nm. Moreover, the material displays temperature-dependent mechanical behavior. Micropillars pyrolyzed at 1000 °C achieve a strength of 6.41 GPa and a failure strain of 30%, while those pyrolyzed at 1200 °C demonstrate increased compressive strength up to 7.55 GPa. To demonstrate practical utility, we fabricate various nanolattice structures and characterize their mechanical perform-

https://doi.org/10.1021/acsnano.6c02930
ACS Nano XXXX, XXX, XXX−XXX

ance. The shell-based architecture, with a relative density of 20%, exhibits a compressive strength as high as 0.54 GPa and a failure strain exceeding 10%. We also produce functional microneedle arrays, highlighting their potential for biomedical applications. Overall, this work not only establishes a reliable pathway for fabricating high-performance PDC microdevices but also offers a general and accessible solution that addresses the trade-offs among precursor simplicity, shape fidelity, and mechanical robustness. This consequently broadens the application prospects of polymer-derived ceramics in fields such as damage-tolerant lightweight metamaterials, biomedical microdevices, and microelectromechanical systems (MEMS).

RESULTS AND DISCUSSION

Photosensitive Preceramic Resin and its TPP Mechanism

Figure 1a illustrates the basic process for the fabrication of PDC microstructures. First, a preceramic resin that can be stored and used over an extended period under ambient conditions (20 °C) is prepared via a straightforward synthetic step [Figure 1a(i)]. Subsequently, 3D preceramic polymer microstructures are fabricated via TPP-based 3D printing, as exemplified by the double-layer fullerene-like structure shown in Figure 1a(ii). After pyrolysis at 1000 °C in an inert gas atmosphere, preceramic polymer is converted to SiOC ceramic. Figure 1a(iii) shows the final double-layer fullerene ceramic microstructure, which exhibits high structural fidelity and is free of defects.

The simplicity and reliability of precursor development are key to the widespread application of TPP-PDC technology. To achieve this, we develop an extremely simple preceramic resin system, and the entire preparation process is also very straightforward. Specifically, a commercially available liquid polycarbosilane is directly used as the single ceramic precursor without any chemical modification. The molecule of polycarbosilane contains vinyl groups (Figure S1, Supporting Information), which provide the basic reactive moieties required for TPP printing. The material requires no additional cross-linkers to assist curing or solvents to dissolve the precursor. Only the photoinitiator ethyl methyl ketone (EMK) is introduced to generate free radicals, accompanied by a small amount of xylene to dissolve the photoinitiator. Subsequently, the mixture is treated ultrasonically in a 40 °C water bath for 20 min to achieve uniform mixing, yielding a photosensitive preceramic resin. As shown in Figure 1a(i), the obtained resin is transparent and clear, which can be stored at ambient conditions for long-term use. Even after over one year of storage, it maintains excellent fluidity and transparency, and can still be processed normally in TPP printing (Figure S2, Supporting Information).

If the prepared photosensitive resin is used directly for TPP printing, the resin exhibits insufficient polymerization degree. We observe that the resin demonstrates high fluidity, and the printed structures are both incomplete and unstable. The polymerized structures tend to disappear during or shortly after fabrication, even when the laser power is increased to overexposure (Figure S3, Supporting Information). We speculate that the polymerization process relies solely on the vinyl functional groups, whose limited photocuring activity results in an insufficient cross-linked network density and consequently leads to structural instability in the polymerized material. To enhance the printing performance of the resin, a prebaking step at 90 °C in air for 10 min is implemented prior to the printing process. The prebaking process enhances the spatial network density and viscosity of the precursor through precross-linking, thereby improving the structural stability of the preceramic polymer formed (Figure 1b). To determine the prebaking conditions, we conduct systematic experiments. When the prebaking cross-linking degree is insufficient, the resin viscosity is low, leading to poorly formed structures prone to collapse and incomplete polymerization during laser direct writing. Conversely, excessive prebaking can cause local precipitation of particles in the resin, affecting the printing process, or lead to overcross-linking, making it difficult to remove unpolymerized parts during development, resulting in nondesigned residual structures. Therefore, we finally determine the optimal prebaking conditions to be heating at 90 °C in air for 10 min. Under these conditions, the viscosity of the preceramic polymer gradually increases (Figure S4, Supporting Information). Subsequently, prebaking forms an appropriate precross-linked network, providing a stable foundation for subsequent high-precision printing.

To investigate the reaction mechanisms during prebaking and photopolymerization, the Fourier Transform Infrared (FTIR) spectra of the original resin, the prebaked resin, and the cured preceramic polymer are systematically tested (Figure 1c). The peaks at 1400 cm^{-1}, 1605 cm^{-1}, and 3055 cm^{-1} result from the characteristic absorption of the C═C group.[29−31] The absorption band at 2102 cm^{-1} can be attributed to Si−H.[32] The C═O stretching vibration observed at 1725 cm^{-1} likely originates from the photoinitiator. The band at 961 cm^{-1} is due to Si−OH, while the vibration at 1035 cm^{-1} is caused by Si−O−Si.[22,33,34] In the original resin, the appearance of Si−OH and Si−O−Si bonds is observed, which is due to the susceptibility of Si−H bonds to hydrolysis and oxidation in air.[33,34] When the sample is heated in air, the absorption peaks for Si−H and Si−OH decrease, while the Si−O−Si absorption peak increase. This indicates that the prebaking process promotes the oxidation of Si−H and the condensation of Si−OH, generating a Si−O−Si network structure and achieving preliminary cross-linking of the precursor. After photocuring, the vinyl groups at 3055, 1400, and 1605 cm^{-1} are observed to be significantly weakened, confirming the successful completion of the photopolymerization reaction. Therefore, the two-step curing mechanism of the preceramic resin is as follows. First, the resin is prebaked in air, where Si−H undergoes thermal oxidation with oxygen, forming a Si−O−Si network structure to achieve precuring, thereby increasing the resin viscosity to improve the stability of structures during subsequent processing. Then, femtosecond laser irradiation completes the final photocuring via vinyl group cross-linking (Figure 1b). The synergistic effect of thermal cross-linking and two-photon curing achieves a precursor network with high cross-linking density and structural stability, providing the foundation for reliable printing. Multiple microstructures are successfully printed, validating the robustness of the fabrication process (Figure 1d).

3D Defect-Free SiOC Ceramic Microstructures and Elemental Composition Analysis

To yield the final SiOC ceramic, the printed 3D preceramic polymer is pyrolyzed at 1000 °C in an argon atmosphere. The pyrolysis process is shown in Figure S5, Supporting Information. To evaluate the processability of the developed preceramic resin and the forming quality of the resulting 3D SiOC ceramic microstructures, we systematically compare the

https://doi.org/10.1021/acsnano.6c02930
ACS Nano XXXX, XXX, XXX−XXX

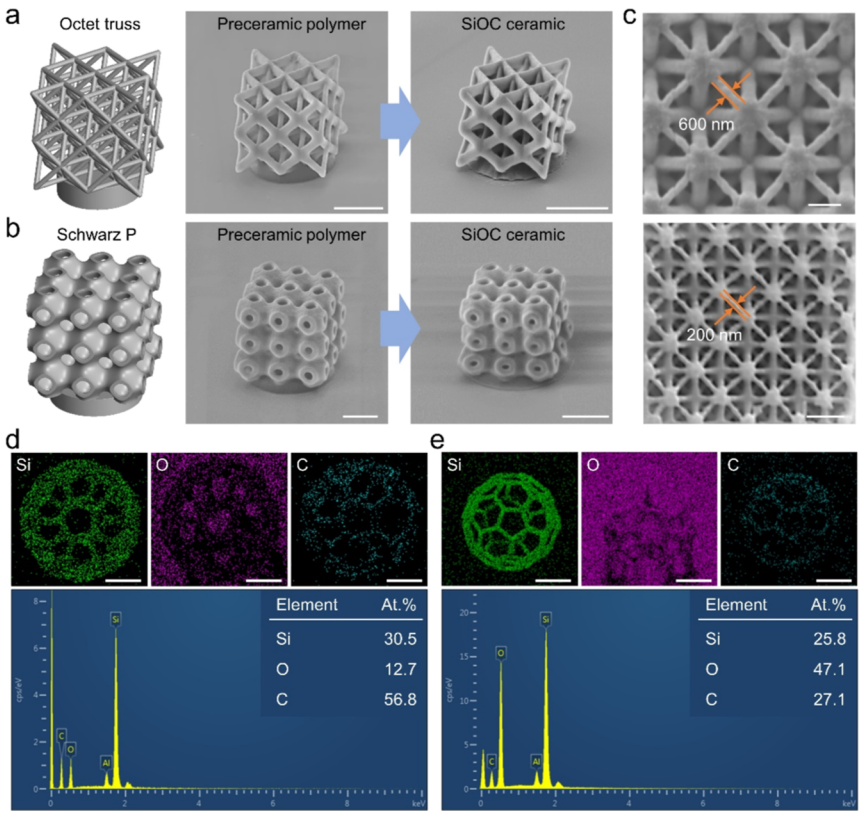

Figure 2. Fabricated 3D SiOC ceramic microstructures and elemental composition analysis. (a-b) The design, printed preceramic polymer structures, and the corresponding pyrolyzed SiOC ceramics 3D microstructures, including (a) Octet truss and (b) Schwarz P. Scale bars, 10 μm. (c) 3D SiOC microstructures with minimum feature sizes of approximately 600 and 200 nm. Scale bars, 2 μm. (d-e) EDS element maps and spectra of (d) the printed preceramic polymer structures and (e) the corresponding pyrolyzed SiOC ceramics 3D microstructures. Scale bars, 10 μm.

morphologies of various 3D structures in their preceramic polymer state and after pyrolysis. Figure 2a and b show the printed preceramic polymer structures and the corresponding pyrolyzed SiOC ceramics, which include octet truss and Schwarz P structures. SEM observations reveal that the pyrolyzed 3D structures exhibit almost no noticeable defects, isotropic shrinkage, and low shrinkage rate (28%). Quantitative dimensional analysis demonstrates that the dimensions of the printed and pyrolyzed structures maintain excellent consistency in both lateral and vertical directions (Figure S6 and Table S1, Supporting Information). More structures are shown in Figure S7, Supporting Information. Furthermore, we demonstrate microstructures with feature sizes as small as 600 and 200 nm, confirming their suitability for nanodevice applications (Figure 2c). These results clearly demonstrate that the resin developed in this work possesses excellent capability for shaping complex and high-precision 3D PDC microstructures, while also showing low shrinkage and good shape retention during pyrolysis. This relatively low shrinkage rate is primarily attributed to the molecular architecture of the precursor polymer itself and the highly dense cross-linked network formed through the two-step cross-linking process. To confirm this, the ceramic yields of the original, prebaked, and cured precursors are measured by thermogravimetric analysis (TGA). The residual ceramic yields at 1000 °C are 49.32%, 57.01%, and 64.50%, respectively (Figure S8, Supporting Information). These quantitative data clearly demonstrate that both prebaking and subsequent curing effectively enhance the cross-linking degree of the preceramic polymer, leading to a significantly increased ceramic yield compared with that of the pristine precursor. Furthermore, we compare our ceramic yields with those reported in the literature for SiOC ceramics. Our yields exceed the majority of previously reported values (Table S2, Supporting Information).[13,14,25,34−43]

It is worth noting that, in addition to the lattice structure with a relative density of 20% demonstrated here, our method is also applicable to lattice structures with higher relative densities or larger feature thicknesses. This is because during pyrolysis, gas diffusion and internal stress are influenced by feature size, but they can be effectively managed by adjusting process parameters such as the ramp rate. To support this, we perform an internal analysis on structures with larger feature thicknesses, as shown in Figure S9, Supporting Information. A solid square structure is fabricated. After pyrolysis, the interior of the structure is sectioned using focused ion beam (FIB) technique, and the resulting images reveal no defects inside the structure. Energy Dispersive X-ray Spectroscopy (EDS) analysis is performed on both the preceramic polymer microstructures (Figure 2d) and the pyrolyzed SiOC ceramics (Figure 2e). The results demonstrate that all elements are homogeneously distributed across the structure. Further quantitative elemental analysis indicates that before pyrolysis, the atomic percentages of Si, O, and C are 30.5%, 12.7%, and 56.8%, respectively (Figure 2d). After pyrolysis, the corresponding values change to 25.8%, 47.1%, and 27.1% (Figure 2e). Although the preceramic polymer is pyrolyzed in an inert atmosphere, the O content remains relatively high. This could be attributed to trace residual oxygen inside the tube furnace,

https://doi.org/10.1021/acsnano.6c02930
ACS Nano XXXX, XXX, XXX−XXX

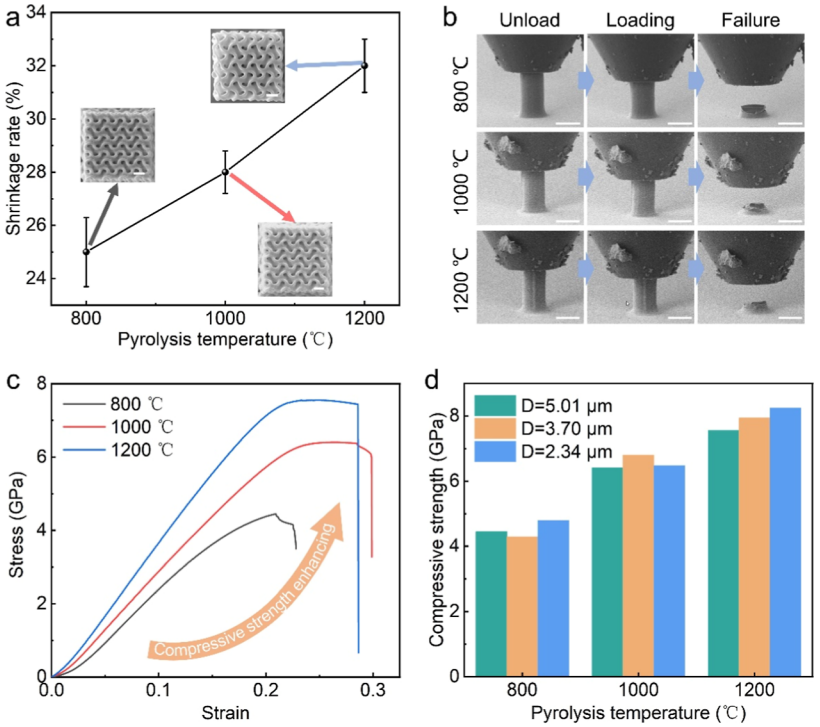

Figure 3. Linear shrinkage rates and mechanical properties of the SiOC microstructures with different pyrolysis temperatures. (a) The SEM images and linear shrinkage rates of the gyroid SiOC microstructures with different pyrolysis temperatures. Scale bars, 2 μm. (b) In situ SEM compression of the SiOC micropillars with a diameter of about 5 μm at different pyrolysis temperatures. Scale bars, 5 μm. (c) Compressive stress−strain curves of the SiOC micropillars with a diameter of about 5 μm at different pyrolysis temperatures. (d) Comparison of compressive strength of micropillars with different diameters and pyrolysis temperatures.

whose influence is more pronounced in micro/nanoscale structures compared with macroscopic samples.[27] Simultaneously, a substantial fraction of the carbon is released as gaseous small molecules during pyrolysis, resulting in the observed decrease in its proportion.

Temperature-Dependent Structural Properties

To study the influence of pyrolysis temperature on the morphology, triply periodic minimal surface (gyroid) structures are printed and subjected to annealing in an argon atmosphere within the temperature range of 800 to 1200 °C. After pyrolysis at different temperatures, the samples exhibit a well-defined morphology with clear outlines and no observable crystallization grains. The linear shrinkage rate slightly increases with rising temperature, approximately 25%, 28%, and 32% at 800 °C, 1000 °C, and 1200 °C, respectively (Figure 3a). Notably, after pyrolysis at 1200 °C, the microstructure becomes markedly smoother and shows a tendency to melt at the contact region between the structure base and the sapphire substrate (Figure S10, Supporting Information). At a pyrolysis temperature of 1300 °C, the structures almost completely collapsed. This is because, when heated to 1200−1400 °C, SiOC undergoes phase separation, forming SiO_2-rich regions and the SiC phase.[44,45] In addition, residual oxygen in the furnace atmosphere inevitably diffuses into the structure during heat treatment, generating an additional SiO_2 phase. EDS analysis of the microstructure pyrolyzed at 1200 °C supports this, showing a significant increase in oxygen content (Figure S11, Supporting Information). When the temperature reaches 1200 °C, it exceeds the glass transition temperature of SiO_2, causing it to transition from a rigid glassy state to a viscous flow state.[46,47] For micro- and nanosized 3D structures, this softening effect is greatly amplified. Their high specific surface area and small curvature radii make surface-tension-driven viscous flow much more severe than that in bulk materials. This leads to rounding of sharp features and ultimately to complete collapse of the structures at higher temperatures, causing irreversible structural failure before crystallization. Similar phenomena have been reported in previous studies.[48−50]

To evaluate the mechanical properties of the SiOC ceramics with different pyrolysis temperature, in situ compression tests are performed on micropillars with a diameter of about 5 μm. Figure 3b presents SEM images capturing the compression process of the micropillars, showing ductile deformation behavior, and the failure process is essentially consistent in all cases, with fracture originating from the base. The stress−strain curves show that these micropillars possess exceptional strength, with a failure strain reaching up to 30% (Figure 3c). Furthermore, with increasing pyrolysis temperature, their compressive strength progressively rises from 4.45 to 7.55 GPa, and the elastic modulus gradually increases from 31.5 to 45.5 GPa (Figure S12, Supporting Information). This indicates that higher pyrolysis temperatures lead to an increased degree of ceramization, a denser microstructure, and a gradual enhancement in mechanical properties. The mechanical properties of micropillars at smaller dimensions are also measured (Figure 3d and Figure S13, Supporting Information). The results demonstrate that they similarly exhibit consistent deformation behavior and high strength, which can be attributed to the defect-free nature of the fabricated structures (Figure S14, Supporting Information). Figure S15 summarizes a comparison of the mechanical properties of micropillars made of different materials reported to

https://doi.org/10.1021/acsnano.6c02930
ACS Nano XXXX, XXX, XXX−XXX

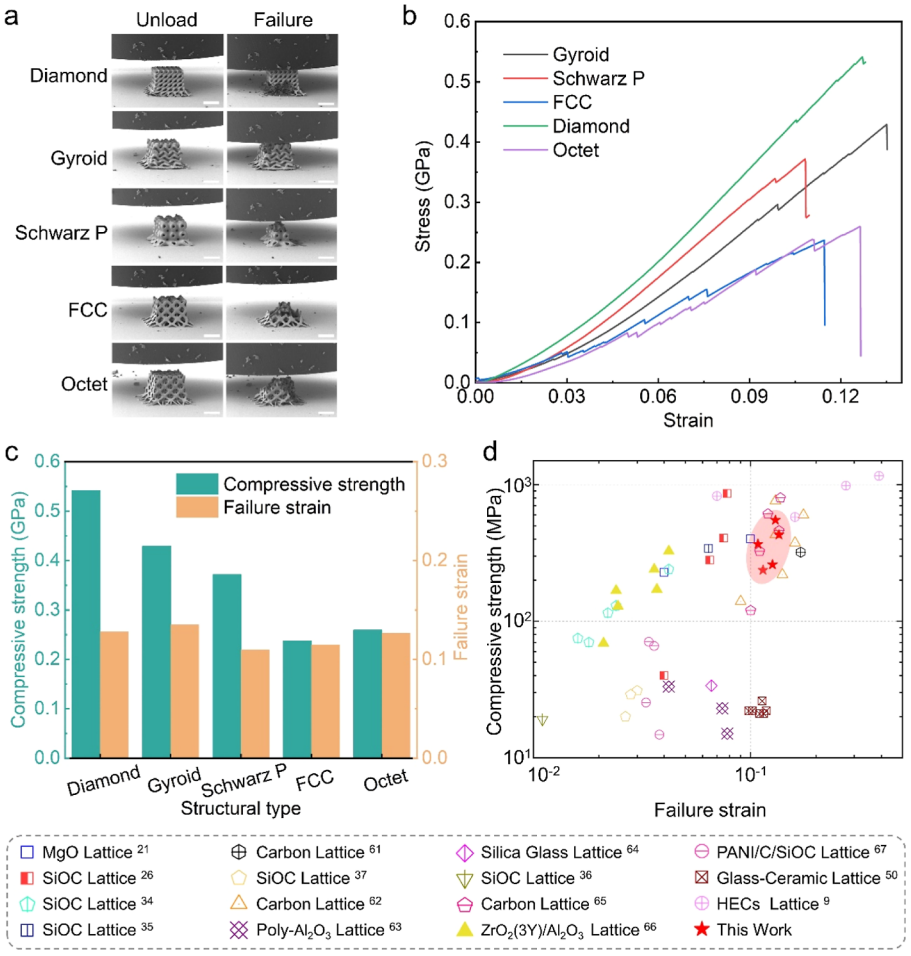

Figure 4. Mechanical properties of SiOC lattices. (a) SEM images before and after compressive failure. Scale bars, 10 μm. (b) Compressive stress−strain curves of the different lattice types. (c) Comparison of compressive strength and failure strain among different lattice types. (d) Comparison of compressive strength and failure strain between our SiOC lattices and other lattice structures reported in the literature for different materials and types.

date.[9,20,26,28,51−60] The specific data are provided in Table S3, Supporting Information. The SiOC micropillars prepared by our method exhibits exceptional strength and toughness, offering broad application prospects.

Mechanical Properties Evaluation and Application of 3D SiOC Microarchitectures

To assess the application potential of this work in the field of lightweight, high-strength materials, two types of lattice structures, including beam-based metamaterials (face-centered cubic (FCC) truss structure and Octet) and shell-based metamaterials (Diamond, Gyroid, and Schwarz P), are designed with the same relative density of 20%. All structures are pyrolyzed at 1000 °C under the argon atmosphere, and their deformation and failure under uniaxial compression are observed (Figure 4a). To obtain reliable and reproducible mechanical data, the structures here are printed directly onto the sapphire substrate, without an additional base layer added at the bottom of the structures as shown in Figure 2. Figure 4b presents the stress−strain curves of these lattice structures, all of which exhibit a good linear relationship and exceptionally high strength, reaching up to 0.54 GPa. Figure 4c provides a detailed comparison of the compressive strength and failure strain of these lattice architectures. The corresponding elastic modulus is shown in Figure S16, Supporting Information. The compressive strength of shell-based mechanical metamaterials is significantly higher than that of beam-based ones. This can be attributed to the smooth and continuous curved-surface geometry of shell-based structures, which effectively reduces stress concentration and thereby imparts superior mechanical performance. In contrast, the damage in beam-based structures tends to concentrate more intensely during compression, which readily leads to catastrophic fracture. Although the fracture stresses differ, the failure strains remain relatively consistent, falling within the range of 10%−15%.

Figure 4d summarizes the compressive strength and failure strain of other structures reported in the literature for different materials and types.[9,21,26,34−37,50,61−67] To enable a more comprehensive comparison of mechanical properties, the density of the ceramic pyrolyzed at 1000 °C is measured. The mass of the samples is determined using a balance, and the volume is measured by the water displacement method, which involves immersing the sample in a graduated cylinder filled with water and recording the volume change. The density of the sample is calculated to be 2.02 g cm^{-3}. Figure S17 summarizes a comparison of compressive strength versus density and elastic modulus versus density between the SiOC ceramic lattices fabricated in this work and other reported lattice structures. The specific data are provided in Table S4, Supporting Information. Owing to their defect-free nature (Figure S18, Supporting Information), excellent mechanical

https://doi.org/10.1021/acsnano.6c02930
ACS Nano XXXX, XXX, XXX−XXX

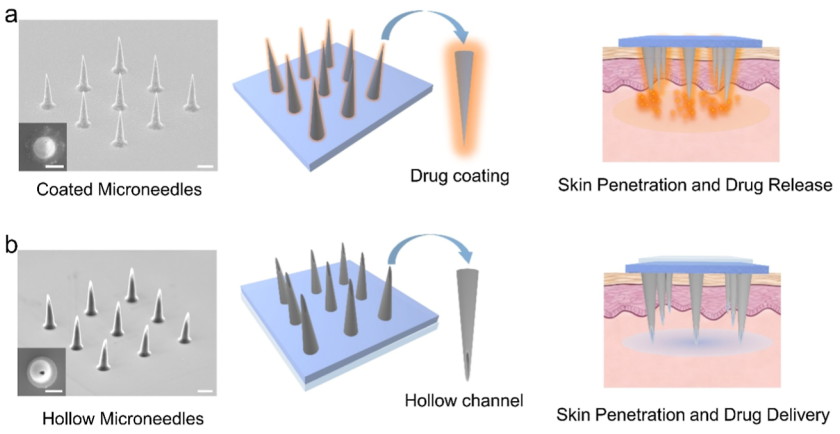

Figure 5. Demonstration of SiOC microneedle arrays. (a) SEM image and working schematic of coated microneedle arrays for drug release. Scale bars, 10 and 5 μm for enlarged SEM image. (b) SEM image and working schematic of hollow microneedle arrays for dual-function applications in interstitial fluid extraction and drug delivery. Scale bars, 10 and 5 μm for enlarged SEM image.

properties, and size effect, the SiOC lattice structures fabricated by our method exhibit exceptionally high strength and enhanced toughness compared with macroscopic-scale lattice architectures. These mechanical properties are comparable to those of the state-of-the-art nanolattice structures produced via TPP reported to date.

Benefiting from its robust mechanical properties and good biocompatibility, SiOC is an ideal material for constructing functional microneedle arrays.[27,68,69] Microneedle technology primarily enables painless, minimally invasive intervention by penetrating the stratum corneum, holding significant application prospects in transdermal drug delivery and point-of-care diagnostics.[70−72] To demonstrate the capability of our approach for precision microneedle fabrication, we successfully produced SiOC ceramic microneedle arrays. As shown in Figure 5a, coated microneedles can release drugs transdermally via surface loading. The hollow microneedles in Figure 5b possess dual functions of extracting interstitial fluid and releasing drugs and can also be used for biomarker monitoring or controlled-release therapy with their fine needle tips. Our method offers high design freedom, enabling the fabrication of complex 3D microneedle geometries (such as gradient needle bodies and multilevel hollow channels) according to specific application requirements and environmental conditions.

To evaluate the biocompatibility of the SiOC microneedle, a cell viability test is performed. HeLa cells are seeded on a glass substrate featuring a fabricated microneedle array and cultured for 36 h (experimental group). As shown in Figure S19, the bright green fluorescence signal indicates that HeLa cells grow and proliferate normally around the microneedle array. A control group was established by culturing HeLa cells on a sapphire substrate without the microneedle array. The fluorescence intensity shows no significant difference between the experimental and control groups, demonstrating that the microneedle array has a negligible impact on HeLa cell viability (Figure S19, Supporting Information). Simultaneously, the penetration capability of the microneedle array was evaluated by pressing it into a polydimethylsiloxane (PDMS) film. It is observed that the microneedles successfully penetrate the PDMS film without fracture (Figure S20, Supporting Information). These tests demonstrate that the fabricated SiOC microneedle arrays hold great potential for biomedical applications.

CONCLUSION

This work establishes a reliable and efficient manufacturing pathway to fabricate high-performance ceramic microdevices from a single preceramic resin. The photosensitive preceramic resin consists solely of polycarbosilane and a photoinitiator, which not only reduces production costs but also significantly enhances ceramic yield, thereby facilitating the minimization of pyrolysis shrinkage. A prebaking-assisted network-densification strategy is introduced for the resin, enabling the construction of robust and stably supported 3D preceramic polymer architectures via TPP printing. Through a pyrolysis process, various 3D SiOC microstructures with high shape fidelity and mechanical robustness are successfully obtained. The micropillars pyrolyzed at 1000 °C exhibit a compressive strength of 6.41 GPa and a failure strain of 30%, while those pyrolyzed at the higher temperature of 1200 °C achieve a compressive strength of 7.55 GPa. The fabricated SiOC nanolattices show a high compressive strength of 0.54 GPa and a high failure strain exceeding 10%, comparable to state-of-the-art TPP-printed ceramic nanolattices reported to date. To highlight the potential biomedical applications of our method, two types of functional microneedle arrays are fabricated, and their biocompatibility and penetration capability are demonstrated. The proposed method integrates simple material processing, good precursor storage stability, high 3D shaping capability, and excellent mechanical properties of the final ceramic. Importantly, it offers a versatile platform readily adoptable by researchers across diverse fields, from micromechanics to biomedicine and from MEMS to extreme-environment materials. By overcoming the conventional challenges of precursor complexity, shrinkage, and compromised mechanical performance, this work establishes a solid foundation for exploring silicon-based ceramics in extreme environments, lightweight structural components, and biomedical microdevices. Future research could further explore fine-tuning precursor chemistry and incorporate various elements to construct more functional ceramic devices, promoting the broader application of polymer-derived ceramics in high-performance 3D micro/nano devices.

https://doi.org/10.1021/acsnano.6c02930
ACS Nano XXXX, XXX, XXX−XXX

EXPERIMENTAL SECTION

Material Preparation

The precursor used in this study is a commercial liquid polycarbosilane (SLF-LPCS, Suzhou Cerafil Ltd., China). 1 wt % photoinitiator ethyl methyl ketone (EMK) was added, together with xylene as solvent at three times the mass of EMK. Afterward, the mixture is treated ultrasonically in a 40 °C water bath for 20 min to obtain the photosensitive preceramic resin (LPCS-EMK). The entire process does not require additional solvent to maintain good fluidity.

Fabrication Process

Prebaking. In the experiment, the resin was first drop-cast onto a sapphire substrate (200 μm) and prebaked on a hot plate at 90 °C in air for 10 min. A thin glass slide (170 μm) was then placed on top, with a 120 μm-thick Kapton tape spacer defining the gap.

TPP Printing. The femtosecond laser source is a mode-locked Ti: sapphire ultrafast oscillator (Chameleon Vision-S, Coherent) with a central wavelength of 800 nm. The pulse width is 75 fs, and the repetition rate is 80 MHz. The laser is tightly focused using a 60× oil objective with high numerical aperture (NA = 1.35) in order to realize high resolution. The laser focus is steered by a pair of galvo-mirrors for 2D scanning, while the step between two layers is realized by a linear nanopositioning. Point-by-point scanning paths are generated from homemade slicing software. The slicing distance for all structures is 160 nm, and the hatching distance is 210 nm. All preceramic polymer microstructures are printed with a laser power of 15 mW. The exposure time for the micropillars is set to 2000 μs to prevent insufficient mechanical strength, which could otherwise lead to tilting and adversely affect the subsequent compression tests. For the other structures, an exposure time of 1000 μs is applied to improve printing efficiency. Finally, the samples are immersed in xylene for 10 min for development to remove uncured resin, followed by cleaning with ethanol for 2 min to obtain the predesigned 3D structures.

Pyrolysis. Pyrolysis is performed in a high-temperature tube furnace, GSL-1700X (Hefei Kejing Material Technology Co., Ltd.). During the process, the heating rate is 1.5 °C min^{-1}. Holding times of 120 and 60 min are set when the temperature reaches 150 and 400 °C, respectively. Then, the temperature was increased to the target temperature (800 °C, 1000 °C, and 1200 °C), held for 1 h, and subsequently cooled to room temperature inside the furnace. The entire pyrolysis process is conducted in an inert argon atmosphere.

Characterization

SEM. SEM images are taken using a secondary electron scanning electron microscope (Zeiss EVO18, Germany) at an accelerating voltage of 10 keV. Before testing, all samples are coated with ~10 nm gold.

EDS. EDS analysis was performed using a Schottky field emission scanning electron microscope (Gemini-SEM 360, Germany) equipped with a Bruker XFlash6160 detector at an accelerating voltage of 10 keV.

Rheology Test. The viscosity changes of the preceramic polymer over time during isothermal treatment at 90 °C is measured using a rotational rheometer (TA Discovery HR-2, USA). The gap distance between the parallel plate fixtures used for the measurement is 700 μm. The measurement is performed at a constant shear rate of 10 s^{-1}.

TGA. TGA is performed using a thermogravimetric analyzer (NETZSCH TG 309 Supreme, Germany) at a heating rate of 20 °C min^{-1} to 1000 °C under an N_2 atmosphere.

FTIR Spectroscopy. FTIR spectra are collected using an FTIR spectrometer Nicolet 8700 (Thermo Scientific, USA) in the range of 400 to 4000 cm^{-1}.

In Situ Compression Testing. Compression tests are performed inside the Gemini-SEM 360 using a NanoFlip nanoindenter (load range, 0 to 50 mN) with a flat-punch diamond tip of 10 μm for micropillars and 100 μm diameter for lattice structures. All tests are conducted at a displacement rate of 50 nm/s and load-displacement curves are recorded.

ASSOCIATED CONTENT

Supporting Information

The Supporting Information is available free of charge at https://pubs.acs.org/doi/10.1021/acsnano.6c02930.

The molecular structure of polycarbosilane; condition of the resin after one year of storage; processing demonstration of unbaked resin; viscosity evolution of the preceramic polymer during isothermal holding at 90 °C; the heating procedure for pyrolysis in an argon atmosphere; measurement of the size of the printed and pyrolyzed microstructures in X, Y, and Z directions; the pyrolyzed SiOC ceramics 3D microstructures; thermogravimetric analysis of original, prebaked, and prebaked and photocured precursors; internal analysis of the structure pyrolyzed at 1000 °C; effect of pyrolysis temperature on the formed structure; EDS element maps and spectra of the 1200 °C pyrolyzed ceramics 3D microstructures; the elastic modulus of SiOC micropillars; in situ SEM compression and compressive stress−strain curves of the SiOC micropillars at different pyrolysis temperatures; magnified SEM images of the SiOC micropillars pyrolyzed at different temperatures; mechanical property comparison of micropillars made of different materials reported to date; the elastic modulus of SiOC lattices; mechanical property comparison of advanced micro/nano lattices reported to date; magnified top-view SEM images of the SiOC 3D lattice structures used for in situ compression tests; the viability test by culturing cells with SiOC microneedle array; SEM images of SiOC microneedles after penetrating the Polydimethylsiloxane membrane; the size and shrinkage rate of the printed and pyrolyzed microstructures in X, Y, and Z directions; comparison of ceramic yields between our method and those reported in the literature; mechanical property comparison between our SiOC micropillars and the micropillars reported in the literature; and mechanical property comparison between our SiOC lattices and the lattice structures reported in the literature (PDF)

AUTHOR INFORMATION

Corresponding Author

Jiawen Li − *CAS Key Laboratory of Mechanical Behavior and Design of Materials, Key Laboratory of Precision Scientific Instrumentation of Anhui Higher Education Institutes, Department of Precision Machinery and Precision Instrumentation, University of Science and Technology of China, Hefei 230027, China; Hefei National Laboratory, University of Science and Technology of China, Hefei 230088, China;* orcid.org/0000-0003-3950-6212; Email: jwl@ustc.edu.cn

Authors

Gan Luo − *CAS Key Laboratory of Mechanical Behavior and Design of Materials, Key Laboratory of Precision Scientific Instrumentation of Anhui Higher Education Institutes, Department of Precision Machinery and Precision Instrumentation, University of Science and Technology of China, Hefei 230027, China*

Yuan Tao − *CAS Key Laboratory of Mechanical Behavior and Design of Materials, Key Laboratory of Precision Scientific*

https://doi.org/10.1021/acsnano.6c02930
ACS Nano XXXX, XXX, XXX−XXX

Instrumentation of Anhui Higher Education Institutes, Department of Precision Machinery and Precision Instrumentation, University of Science and Technology of China, Hefei 230027, China

Jincheng Ni − *CAS Key Laboratory of Mechanical Behavior and Design of Materials, Key Laboratory of Precision Scientific Instrumentation of Anhui Higher Education Institutes, Department of Precision Machinery and Precision Instrumentation, University of Science and Technology of China, Hefei 230027, China*

Modong Jiang − *CAS Key Laboratory of Mechanical Behavior and Design of Materials, Key Laboratory of Precision Scientific Instrumentation of Anhui Higher Education Institutes, Department of Precision Machinery and Precision Instrumentation, University of Science and Technology of China, Hefei 230027, China*

Feng Tang − *CAS Key Laboratory of Mechanical Behavior and Design of Materials, Key Laboratory of Precision Scientific Instrumentation of Anhui Higher Education Institutes, Department of Precision Machinery and Precision Instrumentation, University of Science and Technology of China, Hefei 230027, China*

Yanlei Hu − *CAS Key Laboratory of Mechanical Behavior and Design of Materials, Key Laboratory of Precision Scientific Instrumentation of Anhui Higher Education Institutes, Department of Precision Machinery and Precision Instrumentation, University of Science and Technology of China, Hefei 230027, China;* orcid.org/0000-0003-1964-0043

Dong Wu − *CAS Key Laboratory of Mechanical Behavior and Design of Materials, Key Laboratory of Precision Scientific Instrumentation of Anhui Higher Education Institutes, Department of Precision Machinery and Precision Instrumentation, University of Science and Technology of China, Hefei 230027, China;* orcid.org/0000-0003-0623-1515

Jiaru Chu − *CAS Key Laboratory of Mechanical Behavior and Design of Materials, Key Laboratory of Precision Scientific Instrumentation of Anhui Higher Education Institutes, Department of Precision Machinery and Precision Instrumentation, University of Science and Technology of China, Hefei 230027, China;* orcid.org/0000-0001-6472-8103

Complete contact information is available at: https://pubs.acs.org/10.1021/acsnano.6c02930

Author Contributions

[§]G.L. and Y.T. contributed equally to this work. G.L., Y.T., and J.L. conceived the research. J.L. supervised the research. G.L., Y.T., and M.J. made the precursor resin and fabricated the samples. G.L., Y.T., and M.J. performed characterization. G.L. and M.J. performed mechanical testing. G.L., Y.T., M.J., and F.T. analyzed the data. Y.T. and G.L. wrote the initial manuscript. All authors contributed to the final manuscript and approved the submission.

Notes

The authors declare no competing financial interest.

ACKNOWLEDGMENTS

This work is supported by the National Key Research and Development Program of China (Nos. 2021YFF0502700, 2024YFB4610700), the National Natural Science Foundation of China (Nos. 52075516, 62325507, 62375253, 52375582), Major Scientific and Technological Projects in Anhui Province (Nos. 202103a05020005, 202203a05020014), Hefei Municipal Natural Science Foundation (No. HZR2450), the Independent Deployment Project of HFNL (Grant No. ZB2025010600), and the Fundamental Research Funds for the Central Universities (WK2090050048). We acknowledge the Experimental Center of Engineering and Material Sciences at USTC for the fabrication and measuring of samples. This work is partially carried out at the USTC Center for Micro and Nanoscale Research and Fabrication and Instruments Center for Physical Science, University of Science and Technology of China.

REFERENCES

(1) Huang, Z.; Shao, G.; Li, L. Micro/Nano Functional Devices Fabricated by Additive Manufacturing. *Prog. Mater. Sci.* **2023**, *131*, 101020.

(2) Tancogne-Dejean, T.; Diamantopoulou, M.; Gorji, M. B.; Bonatti, C.; Mohr, D. 3D Plate-Lattices: An Emerging Class of Low-Density Metamaterial Exhibiting Optimal Isotropic Stiffness. *Adv. Mater.* **2018**, *30* (45), 1803334.

(3) Zhang, N.; Wang, Z.; Zhao, Z.; Zhang, D.; Feng, J.; Yu, L.; Lin, Z.; Guo, Q.; Huang, J.; Mao, J.; Yang, J. 3D Printing of Micro-Nano Devices and Their Applications. *Microsyst. Nanoeng.* **2025**, *11* (1), 35.

(4) Hu, S.; Park, C.; Jeong, S.; Jeon, N.; Kim, J. T.; Rho, J. Additive Manufacturing of Metastructures at the Micro- and Nano-Scale. *Chem. Soc. Rev.* **2026**, *55*, 1666−1716.

(5) Meza, L. R.; Zelhofer, A. J.; Clarke, N.; Mateos, A. J.; Kochmann, D. M.; Greer, J. R. Resilient 3D Hierarchical Architected Metamaterials. *Proc. Natl. Acad. Sci. U. S. A.* **2015**, *112* (37), 11502−11507.

(6) Su, R.; Chen, J.; Zhang, X.; Wang, W.; Li, Y.; He, R.; Fang, D. 3D-Printed Micro/Nano-Scaled Mechanical Metamaterials: Fundamentals, Technologies, Progress, Applications, and Challenges. *Small* **2023**, *19* (29), 2206391.

(7) Arshad, Q.; Saqib, M.; Arshad, M. A.; Raza, M.; Hussain, M. I.; Asghar, A.; Luo, X.; Chen, Z. Progress in Vat Photopolymerisation Additive Manufacturing of Ceramic Lattice Structures and Applications. *Thin-Walled Struct.* **2025**, *209*, 112918.

(8) Chen, Z.; Li, Z.; Li, J.; Liu, C.; Lao, C.; Fu, Y.; Liu, C.; Li, Y.; Wang, P.; He, Y. 3D Printing of Ceramics: A Review. *J. Eur. Ceram. Soc.* **2019**, *39* (4), 661−687.

(9) Jiang, M.; Li, R.; Li, B.; Ni, J.; Wang, G.; Zhang, Z.; Chen, Y.; Hu, Y.; Wu, D.; Chu, J.; Wu, H.; Li, J. Lightweight and Ultrastrong 3D Nanoarchitected High-Entropy Ceramic Metamaterials. *Sci. Adv.* **2025**, *11* (42), No. eadw6632.

(10) Colombo, P.; Mera, G.; Riedel, R.; Soraru, G. D. Polymer-Derived Ceramics: 40 Years of Research and Innovation in Advanced Ceramics. *J. Am. Ceram. Soc.* **2010**, *93* (7), 1805−1837.

(11) Chaudhary, R. P.; Parameswaran, C.; Idrees, M.; Rasaki, A. S.; Liu, C.; Chen, Z.; Colombo, P. Additive Manufacturing of Polymer-Derived Ceramics: Materials, Technologies, Properties and Potential Applications. *Prog. Mater. Sci.* **2022**, *128*, 100969.

(12) Lacelle, T.; Sampson, K. L.; Yazdani Sarvestani, H.; Rahimizadeh, A.; Barroeta Robles, J.; Mirkhalaf, M.; Rafiee, M.; Jakubinek, M. B.; Paquet, C.; Ashrafi, B. Additive Manufacturing of Polymer Derived Ceramics: Materials, Methods, and Applications. *APL Mater.* **2023**, *11* (7), 070602.

(13) Eckel, Z. C.; Zhou, C.; Martin, J. H.; Jacobsen, A. J.; Carter, W. B.; Schaedler, T. A. Additive Manufacturing of Polymer-Derived Ceramics. *Science* **2016**, *351* (6268), 58−62.

(14) Zanchetta, E.; Cattaldo, M.; Franchin, G.; Schwentenwein, M.; Homa, J.; Brusatin, G.; Colombo, P. Stereolithography of SiOC Ceramic Microcomponents. *Adv. Mater.* **2016**, *28* (2), 370−376.

https://doi.org/10.1021/acsnano.6c02930
ACS Nano XXXX, XXX, XXX−XXX

(15) Zhou, S.; Mei, H.; Chang, P.; Lu, M.; Cheng, L. Molecule Editable 3D Printed Polymer-Derived Ceramics. *Coord. Chem. Rev.* **2020**, *422*, 213486.
(16) Ackley, B. J.; Martin, K. L.; Key, T. S.; Clarkson, C. M.; Bowen, J. J.; Posey, N. D.; Ponder, J. F., Jr.; Apostolov, Z. D.; Cinibulk, M. K.; Pruyn, T. L.; Dickerson, M. B. Advances in the Synthesis of Preceramic Polymers for the Formation of Silicon-Based and Ultrahigh-Temperature Non-Oxide Ceramics. *Chem. Rev.* **2023**, *123* (8), 4188−4236.
(17) Vyatskikh, A.; Delalande, S.; Kudo, A.; Zhang, X.; Portela, C. M.; Greer, J. R. Additive Manufacturing of 3D Nano-Architected Metals. *Nat. Commun.* **2018**, *9* (1), 593.
(18) Yee, D. W.; Lifson, M. L.; Edwards, B. W.; Greer, J. R. Additive Manufacturing of 3D-Architected Multifunctional Metal Oxides. *Adv. Mater.* **2019**, *31* (33), 1901345.
(19) Zhou, X.; Liu, X.; Gu, Z. Photoresist Development for 3D Printing of Conductive Microstructures via Two-Photon Polymerization. *Adv. Mater.* **2024**, *36* (48), 2409326.
(20) Bauer, J.; Crook, C.; Baldacchini, T. A Sinterless, Low-Temperature Route to 3D Print Nanoscale Optical-Grade Glass. *Science* **2023**, *380* (6648), 960−966.
(21) Jiang, M.; Qu, L.; Tao, Y.; Ni, J.; Hu, Y.; Wu, D.; Chu, J.; Li, J. 3D Nanoprinting of Multifunctional MgO Transparent Ceramics. *ACS Nano* **2025**, *19* (20), 19318−19327.
(22) Tao, Y.; Gu, X.; Wu, H.; Ni, J.; Hu, Y.; Wu, D.; Chu, J.; Li, J. Ultralow Shrinkage 3D Transparent Nanoporous Glass Printing through Low-Temperature Sintering for Micro-Optical Applications. *ACS Nano* **2025**, *19* (35), 31643−31655.
(23) Pham, T. A.; Kim, D. P.; Lim, T. W.; Park, S. H.; Yang, D. Y.; Lee, K. S. Three-Dimensional SiCN Ceramic Microstructures via Nano-Stereolithography of Inorganic Polymer Photoresists. *Adv. Funct. Mater.* **2006**, *16* (9), 1235−1241.
(24) Park, S.; Lee, D. H.; Ryoo, H. I.; Lim, T. W.; Yang, D. Y.; Kim, D. P. Fabrication of Three-Dimensional SiC Ceramic Microstructures with Near-Zero Shrinkage via Dual Crosslinking Induced Stereolithography. *Chem. Commun.* **2009**, No. 32, 4880−4882.
(25) Brigo, L.; Schmidt, J. E. M.; Gandin, A.; Michieli, N.; Colombo, P.; Brusatin, G. 3D Nanofabrication of SiOC Ceramic Structures. *Adv. Sci.* **2018**, *5* (12), 1800937.
(26) Bauer, J.; Crook, C.; Guell Izard, A.; Eckel, Z. C.; Ruvalcaba, N.; Schaedler, T. A.; Valdevit, L. Additive Manufacturing of Ductile, Ultrastrong Polymer-Derived Nanoceramics. *Matter* **2019**, *1* (6), 1547−1556.
(27) Konstantinou, G.; Kakkava, E.; Hagelüken, L.; Warriam Sasikumar, P. V.; Wang, J.; Makowska, M. G.; Blugan, G.; Nianias, N.; Marone, F.; Van Swygenhoven, H.; Brugger, J.; Psaltis, D.; Moser, C. Additive Manufacturing of Crack-Free PDCs by Two-Photon Polymerization of a Single, Low-Shrinkage Preceramic Resin. *Addit. Manuf.* **2020**, *35*, 101343.
(28) Dang, Y.; Xu, Z.; Yeung, K.-W.; Zhu, Z.; Sun, J.; To, S.; Tang, C.-Y.; Song, Y.; Ruan, H. Nano/Micro-Structured Polymer-Derived SiBCN Ceramics via Two-Photon Lithography. *Addit. Manuf.* **2025**, *109*, 104849.
(29) Kim, S.; Biju, C.; Karunarathna, M. S.; Grimes, N. Y.; Hmeidat, N. S.; Reyes-Zacarias, J.; Agarwal, S.; Anisur Rahman, M.; Gilmer, D. B.; Compton, B. G.; Bullock, S. E.; Saito, T.; Cramer, C. L. Tuning Crosslinking of Hybrid Preceramic Polymers in Vat Photopolymerization toward Controlled Ceramic Yields. *Chem. Eng. J.* **2024**, *499*, 156585.
(30) Gong, J.; Wang, Y.; Zhou, M.; Pei, X.; Huang, J.; Huang, Z.; Huang, Q. Rapid Curing of Liquid Polycarbosilane and Its Conversion into Protective Coating. *Silicon* **2023**, *15* (13), 5803−5810.
(31) Qian, B.; Cao, B.; Chu, M.; Li, Y.; Ma, H.; Guo, R.; Wan, L. Curing Reactions of Liquid Hydridopolycarbosilanes with Vinyl or Allyl Groups. *J. Appl. Polym. Sci.* **2023**, *140* (42), No. e54565.
(32) Liu, H.; Mei, D.; Qian, S.; Wang, Y. Vat Photopolymerization of Polymer-Derived SiC Ceramic with Triply Periodic Minimal Surface Structure for Hydrogen Production. *Addit. Manuf.* **2023**, *73*, 103694.
(33) de Hazan, Y.; Penner, D. SiC and SiOC Ceramic Articles Produced by Stereolithography of Acrylate Modified Polycarbosilane Systems. *J. Eur. Ceram. Soc.* **2017**, *37* (16), 5205−5212.
(34) He, X.; Wang, R.; Qi, S.; Cheng, J.; Ye, H.; Li, H.; Chen, S.; Jian, B.; Ge, Q. Vat Photopolymerization 3D Printing of Polymer-Derived SiOC Ceramics with High Precision and High Strength. *Addit. Manuf.* **2023**, *78*, 103889.
(35) Chen, H.; Chen, X.; Lim, J. S. K.; Lu, Y.; Hu, J.; Liang, Y. N.; Hu, X. M. High-Precision 3D Printing of High-Strength Polymer-Derived Ceramics: Impact of Precursor's Molecular Structure. *Adv. Eng. Mater.* **2022**, *24* (11), 2200269.
(36) Li, Z.; Chen, Z.; Liu, J.; Fu, Y.; Liu, C.; Wang, P.; Jiang, M.; Lao, C. Additive Manufacturing of Lightweight and High-Strength Polymer-Derived SiOC Ceramics. *Virtual Phys. Prototyp.* **2020**, *15* (2), 163−177.
(37) Su, R.; Chen, J.; Zhang, X.; Gao, X.; Wang, W.; Li, Y.; He, R. Accuracy Controlling and Mechanical Behaviors of Precursor-Derived Ceramic SiOC Microlattices by Projection Micro Stereolithography (PμSL) 3D Printing. *J. Adv. Ceram.* **2023**, *12* (11), 2134−2147.
(38) Zhu, N.; Hou, Y.; Yang, W.; Wen, G.; Zhong, C.; Wang, D.; Liu, Y.; Zhang, L. Preparation of Complex SiOC Ceramics by a Novel Photocurable Precursor with Liquid Crystal Display (LCD) 3D Printing Technology. *J. Eur. Ceram. Soc.* **2022**, *42* (7), 3204−3212.
(39) Yazdani, S. H.; Karamzadeh, V.; Kulkarni, A.; Sohrabi-Kashani, A.; Lacelle, T.; Jakubinek, M. B.; Ashrafi, B. High-Performance Polymer-Derived Ceramics in LCD 3D Printing. *Adv. Sci.* **2025**, *12* (18), 2416176.
(40) Zhou, R.; Wang, Y.; Liu, Z.; Pang, Y.; Chen, J.; Kong, J. Digital Light Processing 3D-Printed Ceramic Metamaterials for Electromagnetic Wave Absorption. *Nano-Micro Lett.* **2022**, *14* (1), 122.
(41) Lu, J.; Jing, J.; Zhou, X.; Han, G.; Zhang, Z.; Gong, H.; Wang, X.; Wang, G.; Miao, Y.; Sheng, M.; et al. Vat Photopolymerization 3D Printing Gyroid Meta-Structural SiOC Ceramics Achieving Full Absorption of X-Band Electromagnetic Wave. *Addit. Manuf.* **2023**, *78*, 103827.
(42) Zhao, X.; Li, J.; Li, N.; Wei, L.; Zhang, L.; Zhang, S.; Lei, H. Polymer-Derived SiOC Ceramics by Digital Light Processing-Based Additive Manufacturing. *Appl. Sci.* **2025**, *15* (6), 2921.
(43) Huang, K.; Elsayed, H.; Franchin, G.; Colombo, P. Complex SiOC Ceramics from 2D Structures by 3D Printing and Origami. *Addit. Manuf.* **2020**, *33*, 101144.
(44) Guo, L.; Ma, Q.; Hu, Z.; Xu, C. High-Temperature Evolution Behavior of MK Silicon Resin Derived SiOC Ceramics under Different Environments. *Ceram. Int.* **2021**, *47* (15), 21815−21821.
(45) Stabler, C.; Célarié, F.; Rouxel, T.; Limbach, R.; Wondraczek, L.; Riedel, R.; Ionescu, E. Effect of Composition and High-Temperature Annealing on the Local Deformation Behavior of Silicon Oxycarbides. *J. Eur. Ceram. Soc.* **2019**, *39* (7), 2287−2296.
(46) Rouxel, T.; Massouras, G.; Sorarù, G. D. High Temperature Behavior of a Gel-Derived SiOC Glass: Elasticity and Viscosity. *J. Sol-Gel Sci. Technol.* **1999**, *14* (1), 87−94.
(47) Stabler, C.; Ionescu, E.; Graczyk-Zajac, M.; Gonzalo-Juan, I.; Riedel, R. Silicon Oxycarbide Glasses and Glass-Ceramics: "All-Rounder" Materials for Advanced Structural and Functional Applications. *J. Eur. Ceram. Soc.* **2018**, *101* (11), 4817−4856.
(48) Gailevičius, D.; Padolskytė, V.; Mikoliūnaitė, L.; Šakirzanovas, S.; Juodkazis, S.; Malinauskas, M. Additive-Manufacturing of 3D Glass-Ceramics down to Nanoscale Resolution. *Nanoscale Horiz.* **2019**, *4* (3), 647−651.
(49) Wen, X.; Zhang, B.; Wang, W.; Ye, F.; Yue, S.; Guo, H.; Gao, G.; Zhao, Y.; Fang, Q.; Nguyen, C.; Zhang, X.; Bao, J.; Robinson, J. T.; Ajayan, P. M.; Lou, J. 3D-Printed Silica with Nanoscale Resolution. *Nat. Mater.* **2021**, *20* (11), 1506−1511.
(50) Chai, N.; Yue, Y.; Chen, X.; Zeng, Z.; Li, S.; Wang, X. Isotropic Sintering Shrinkage of 3D Glass-Ceramic Nanolattices: Backbone Preforming and Mechanical Enhancement. *Int. J. Extreme Manuf.* **2024**, *6* (2), 025003.

https://doi.org/10.1021/acsnano.6c02930
ACS Nano XXXX, XXX, XXX−XXX

(51) Zhang, W.; Li, Z.; Dang, R.; Tran, T. T.; Gallivan, R. A.; Gao, H.; Greer, J. R. Suppressed Size Effect in Nanopillars with Hierarchical Microstructures Enabled by Nanoscale Additive Manufacturing. *Nano Lett.* **2023**, *23* (17), 8162−8170.
(52) Bauer, J.; Guell, I. A.; Zhang, Y.; Baldacchini, T.; Valdevit, L. Programmable Mechanical Properties of Two-Photon Polymerized Materials: From Nanowires to Bulk. *Adv. Mater. Technol.* **2019**, *4* (9), 1900146.
(53) Winczewski, J. P.; Zeiler, S.; Gabel, S.; Susarrey-Arce, A.; Gardeniers, J. G. E.; Merle, B. Exploring the Mechanical Properties of Additively Manufactured Carbon-Rich Zirconia 3D Microarchitectures. *Mater. Des.* **2023**, *232*, 112142.
(54) Winczewski, J. P.; Zeiler, S.; Gabel, S.; Maestre, D.; Merle, B.; Gardeniers, J. G. E.; Susarrey Arce, A. Additive Manufacturing of 3D Yttria-Stabilized Zirconia Microarchitectures. *Mater. Des.* **2024**, *238*, 112701.
(55) Han, C.; Li, R.; Jiang, M.; Huang, K.; Tao, Y.; Wang, D.; Wang, G.; Ni, J.; Hu, Y.; Wu, D.; Chu, J.; Li, J. 3D Printing of Metal and Alloy Nanoarchitectures through a Complexation-Driven Strategy. *Nano Lett.* **2025**, *25* (20), 8294−8302.
(56) Fang, W.; Mu, Z.; He, Y.; Kong, K.; Jiang, K.; Tang, R.; Liu, Z. Organic-Inorganic Covalent-Ionic Molecules for Elastic Ceramic Plastic. *Nature* **2023**, *619* (7969), 293−299.
(57) Kulikowski, J.; Delghandi, D.; Wu, C.; Figueroa, S. D.; Cunningham, W. S.; Gianola, D. S.; Portela, C. M.; Gu, X. W. Mechanical Behavior of Nanocluster-Based Nanocomposites Made Using Two-Photon Lithography. *ACS Appl. Mater. Interfaces* **2025**, *17* (23), 34582−34591.
(58) Guruprasad, T. S.; Keryvin, V.; Kermouche, G.; Marthouret, Y.; Sao-Joao, S. Compressive Behaviour of Carbon Fibres Micropillars by in Situ SEM Nanocompression. *Compos. Part A Appl. Sci. Manuf.* **2023**, *173*, 107699.
(59) Zheng, L.; Liang, H.; Tang, J.; Zheng, Q.; Chen, F.; Wang, L.; Li, Q. Micrometer-Scale Poly(ethylene glycol) with Enhanced Mechanical Performance. *Nat. Commun.* **2025**, *16* (1), 4391.
(60) Zhang, X.; Zhong, L.; Mateos, A.; Kudo, A.; Vyatskikh, A.; Gao, H.; Greer, J. R.; Li, X. Theoretical Strength and Rubber-like Behaviour in Micro-Sized Pyrolytic Carbon. *Nat. Nanotechnol.* **2019**, *14* (8), 762−769.
(61) Serles, P.; Yeo, J.; Haché, M.; Demingos, P. G.; Kong, J.; Kiefer, P.; Dhulipala, S.; Kumral, B.; Jia, K.; Yang, S.; Feng, T.; Jia, C.; Ajayan, P. M.; Portela, C. M.; Wegener, M.; Howe, J.; Singh, C. V.; Zou, Y.; Ryu, S.; Filleter, T. Ultrahigh Specific Strength by Bayesian Optimization of Carbon Nanolattices. *Adv. Mater.* **2025**, *37* (14), 2410651.
(62) Zhang, X.; Vyatskikh, A.; Gao, H.; Greer, J. R.; Li, X. Lightweight, Flaw-Tolerant, and Ultrastrong Nanoarchitected Carbon. *Proc. Natl. Acad. Sci. U. S. A.* **2019**, *116* (14), 6665−6672.
(63) Bauer, J.; Hengsbach, S.; Tesari, I.; Schwaiger, R.; Kraft, O. High-Strength Cellular Ceramic Composites with 3D Microarchitecture. *Proc. Natl. Acad. Sci. U. S. A.* **2014**, *111* (7), 2453−2458.
(64) Li, Z.; Jia, Y.; Duan, K.; Xiao, R.; Qiao, J.; Liang, S.; Wang, S.; Chen, J.; Wu, H.; Lu, Y.; Wen, X. One-Photon Three-Dimensional Printed Fused Silica Glass with Sub-Micron Features. *Nat. Commun.* **2024**, *15* (1), 2689.
(65) Wang, Y.; Zhang, X.; Li, Z.; Gao, H.; Li, X. Achieving the Theoretical Limit of Strength in Shell-Based Carbon Nanolattices. *Proc. Natl. Acad. Sci. U. S. A.* **2022**, *119* (34), No. e2119536119.
(66) Zhang, L.; Liu, H.; Yao, H.; Zeng, Y.; Chen, J. 3D Printing of Hollow Lattice Structures of ZrO2(3Y)/Al2O3 Ceramics by Vat Photopolymerization: Process Optimization, Microstructure Evolution and Mechanical Properties. *J. Manuf. Processes.* **2022**, *83*, 756−767.
(67) Arango-Ospina, M.; Xie, F.; Gonzalo-Juan, I.; Riedel, R.; Ionescu, E.; Boccaccini, A. R. Silicon Oxycarbide Based Materials for Biomedical Applications. *Appl. Mater. Today* **2020**, *18*, 100482.
(68) Vallachira Warriam Sasikumar, P.; Müller, E.; Clement, P.; Jang, J.; Kakkava, E.; Panusa, G.; Psaltis, D.; Maniura-Weber, K.; Rottmar, M.; Brugger, J.; Blugan, G. In Vitro Cytocompatibility Assessment of Ti-Modified, Silicon-Oxycarbide-Based, Polymer-Derived, Ceramic-Implantable Electrodes under Pacing Conditions. *ACS Appl. Mater. Interfaces* **2020**, *12* (15), 17244−17253.
(69) Tamayo, A.; Mazo, M. A.; Ruiz-Caro, R.; Martín-Illana, A.; Bedoya, L. M.; Veiga-Ochoa, M. D.; Rubio, J. Mesoporous Silicon Oxycarbide Materials for Controlled Drug Delivery Systems. *Chem. Eng. J.* **2015**, *280*, 165−174.
(70) Kavaldzhiev, M.; Perez, J. E.; Ivanov, Y.; Bertoncini, A.; Liberale, C.; Kosel, J. Biocompatible 3D Printed Magnetic Micro Needles. *Biomed. Phys. Eng. Express* **2017**, *3* (2), 025005.
(71) Detamornrat, U.; McAlister, E.; Hutton, A. R.; Larrañeta, E.; Donnelly, R. F. The Role of 3D Printing Technology in Microengineering of Microneedles. *Small* **2022**, *18* (18), 2106392.
(72) Olowe, M.; Parupelli, S. K.; Desai, S. A Review of 3D-Printing of Microneedles. *Pharmaceutics* **2022**, *14* (12), 2693.

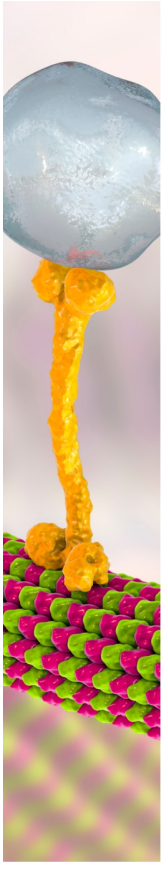

https://doi.org/10.1021/acsnano.6c02930
ACS Nano XXXX, XXX, XXX−XXX